1994A&A...282..151H

Astron. Astrophys. 282, 151–167 (1994)

ASTRONOMY AND ASTROPHYSICS

NLTE model stellar atmospheres with line blanketing near the series limits

I. Hubeny[1], **D. G. Hummer**[2,3], **and T. Lanz**[4,*]

[1] Universities Space Research Association (USRA), NASA Goddard Space Flight Center, Code 681, Greenbelt, MD 20771, USA
[2] Max-Planck-Institut für Astrophysik, Karl-Schwarzschild-Str. 1, D-85748 Garching bei München, Germany
[3] Institut für Astronomie und Astrophysik, Scheinerstr. 1, D-81679 München, Germany
[4] Laboratory for Astronomy and Solar Physics, NASA Goddard Space Flight Center, Code 681, Greenbelt, MD 20771, USA

Received May 17, accepted August 10, 1993

Abstract. In this paper we study the influence of line-merging regions at the immediate long-wavelength side of a continuum threshold on the computed model atmosphere structure and predicted spectrum. In order to model these regions sufficiently accurately, we have developed two concepts. First, we have extended the occupation probability formalism of Hummer and Mihalas to non-LTE plasmas. Second, in order to treat the very complicated opacity in the line merging region, we have generalized the concept of opacity distribution functions to treat non-LTE situations. All Rydberg states are consistently included within this framework, so that no arbitrary cutoff of high (LTE) levels is made. We have calculated several pure hydrogen models atmospheres for two effective temperatures, $T_{\rm eff}$ = 20000 and 35000 K, and discussed the differences between models calculated with various treatments of the line merging. In particular, we have shown that the error in the predicted profiles of Balmer lines resulting from the neglect of line merging is typically of the order of 3 - 4 %, while the errors in the far-UV portion of the Balmer continuum reaches 15 - 35 %. The errors generally decrease with increasing effective temperature. At the same time, the internal accuracy of the models is shown to be about or below 0.5% for all predicted spectral feautures. We conclude that for interpreting current high-accuracy spectrophotometric observations models including the line merging are necessary, and that the formalism developed in this paper is capable of providing a sufficiently accurate and robust modeling technique.

Key words: line formation – radiative transfer – stars: atmospheres, early-type – ultraviolett: stars

1. Introduction

The dramatic improvements in photometric sensitivity and accuracy of stellar spectroscopy in recent years necessitate corresponding improvements in the models used to interpret the spectra. Great advances have been made in improving the physical basis of these models, which together with corresponding developments in computational algorithms have led to a much improved understanding of the nature of stars. These developments for hot stars have been summarized recently by Kudritzki & Hummer (1990). However systematic errors arise in modeling from the need to use only finite numbers of frequency and depth points, as well as of atomic levels and transitions. These restrictions limit the accuracy with which well known physical phenomena can be treated.

The region of line merging on the immediate long-wavelength side of a continuum threshold involves extremely complex physics, which has traditionally been modeled in a rather cavalier manner. But since errors in the representing the opacity and radiation field in this region can affect the flux in *bands much wider than any spectral line*, they are potential sources of significant errors in the temperature distribution. The regions of line merging are complicated for two reasons: 1) the large density of lines and the consequent overlap couples the radiation field in many lines; 2) as high-lying atomic levels are strongly perturbed they are broadened and finally dissolved. These considerations are also crucial in evaluating the internal partition function, although in the present paper this plays a minor role.

The dissolution of high-lying atomic levels by plasma perturbations has been treated by a number of authors in terms of *occupation probabilities*, which for LTE plasmas can be defined as the ratio of the level populations to those in the absence of perturbations. A phenomenological theory for these quantities has been given by Hummer & Mihalas (1988 – hereafter HM), who discuss at length earlier work in this area. Expressions for the optical properties of the plasma in terms of occupation probabilities have been given by Däppen et al. (1987 – hereafter DAM). Seaton (1990) has extended these results by developing a line-broadening theory that goes over smoothly into line dissolution as the strength of the perturbations increases. These

Send offprint requests to: I. Hubeny
* Fellow of the Swiss National Science Foundation

© European Southern Observatory • Provided by the NASA Astrophysics Data System

1994A&A...282..151H

theories have received strong support from the agreement of their predictions with laboratory plasmas and observed spectra of white dwarfs (Bergeron et al. 1991).

In this paper we extend the use of occupation probabilities to non-LTE plasmas. This extension represents a non-trivial generalization of the LTE theory, as the equations of statistical equilibrium must be generalized in a unique and unambiguous manner, i.e. more is involved than arbitrarily multiplying level populations by occupation probabilities. Moreover, we use expressions for occupations probabilities generalized from those of HM to account for electron correlation in the plasma as well as radiator charge. Finally, in order to treat numerically the very complicated opacity in the line-merging region, we have developed a new approach based on the concept of opacity distribution function.

The resulting description of the upper levels of the higher Lyman and Balmer series is used to compute several pure hydrogen model atmospheres with $T_{\rm eff}$= 20000 and 35000 K. These are used as standards to judge the accuracy of various approximations and numerical treatments.

2. Level dissolution in non-LTE plasmas

2.1. Physical basis of the occupation probability formalism

As discussed by HM and DAM, the conceptual basis of the occupation probability picture can be expressed by writing the LTE population of level i as

$$n_i^*/N_{\rm tot} = w_i g_i \exp(-E_i/kT)/Z, \qquad (2.1)$$

where w_i is the occupation probability of level i, g_i the statistical weight, E_i the excitation energy of level i, and Z the internal partition function. The asterisk denotes the equilibrium (LTE) population. Physically, w_i is the probability that the atom in question is in state i relative to that in a similar ensemble of non-interacting atoms. (Throughout we refer to the species in question as an atom, regardless of its charge state.) Correspondingly, $(1 - w_i)$ is the probability that the state i is dissolved, i.e. lies in the continuum. The essential approximation is that a certain fraction of the atoms in level i are completely unaffected, while the remainder are unable to support a bound state at the corresponding energy. The detailed physics is discussed by HM.

Consequently, the wavefunctions and energy eigenvalues of the undissolved atom are just those in the absence of perturbations. Thus the oscillator strengths and other atomic transition rates remain unchanged; the only concept which is changed is the interpretation of the final state of an atomic transition. Now a transition from a certain state i to another state j, $j > i$, may leave an atom either in the bound (undissolved) state j, or in the ionized state at the same energy (i.e. in a certain state of the next higher ion plus free electron), if the state j is dissolved. More precisely, in an ensemble of identical atoms, the transition $i \rightarrow j$ will leave a certain fraction of atoms in bound state j and the complementary fraction in an ionized state at the same energy (dissolved state j).

It follows from (2.1) that the partition function in this picture is (HM)

$$Z = \sum_{i=1}^{\infty} w_i g_i \exp(-E_i/kT). \qquad (2.2)$$

Since w_i monotonically decreases with i, and quickly approaches zero when i exceeds some value depending on the local conditions, this expression avoids the divergence of the classical partition function, as well as with artificial cutoff procedures.

The Saha ionization equation can then be written in the usual form, viz.

$$N_J/N_{J+1} = n_{\rm e}(Z_J/2Z_{J+1})(h^2/2\pi mkT)^{3/2} \exp(\chi_J/kT), \qquad (2.3)$$

where the partition functions are defined through (2.2), i.e. they reflect the dissolution of certain states. Since level dissolution is accounted for in the partition functions, the lowering of the ionization potentials, which is ill–defined (see the discussion in HM), does not appear. In Eq. (2.3), χ_J is the free-atom ionization potential, and all other quantities have their usual meanings.

In order to demonstrate the role of level dissolution in a realistic stellar atmosphere, we display in Fig. 1 the dissolution probabilities $(1 - w_n)$ for the first 80 levels of hydrogen for a pure-hydrogen model atmosphere with $T_{\rm eff}$= 20000 K, and $\log g = 4$, as a function of the principal quantum number and the depth in the atmosphere (in g/cm^2). The latter reflects the dependence of the occupation probability on temperature and electron density.

2.2. Opacity and emissivity

Expressions for opacities and emissivities in the occupation probability formalism, assuming LTE, have been already given by DAM. We now generalize their formalism to non–LTE situations.

The absorption coefficient of atoms in level i (temporarily ignoring stimulated emission) at frequency ν due to all possible transitions $i \rightarrow j$, ($E_j > E_i$ – we will denote this property as $j > i$), including bound–free absorption, is given by

$$\chi_i^{\rm abs}(\nu) = n_i \left\{ \frac{\pi e^2}{mc} \sum_{j>i} \left[w_j \frac{df_{ij}}{d\nu} + (1 - w_j) \frac{df_{ij}}{d\nu} \right] + \sigma_{i\kappa}(\nu) \right\} \qquad (2.4)$$

The first and second terms in the square brackets, respectively, represent transitions to the *undissolved* (bound) part of state j, which occurs with probability w_j (type a in the notation of DAM), and to the *dissolved* component of state j at the same energy (with probability $1 - w_j$); the latter is a bound–free transition extrapolated below the unperturbed threshold(type b of DAM). The last term represent the opacity due to true bound–free transitions. This expression refers to only the undissolved (i.e. existing) atoms in state i. The transitions from a *dissolved* state i to a higher (also dissolved) state j are free–free transitions, and are automatically included in the free–free opacity.

© European Southern Observatory • Provided by the NASA Astrophysics Data System

1994A&A...282..151H

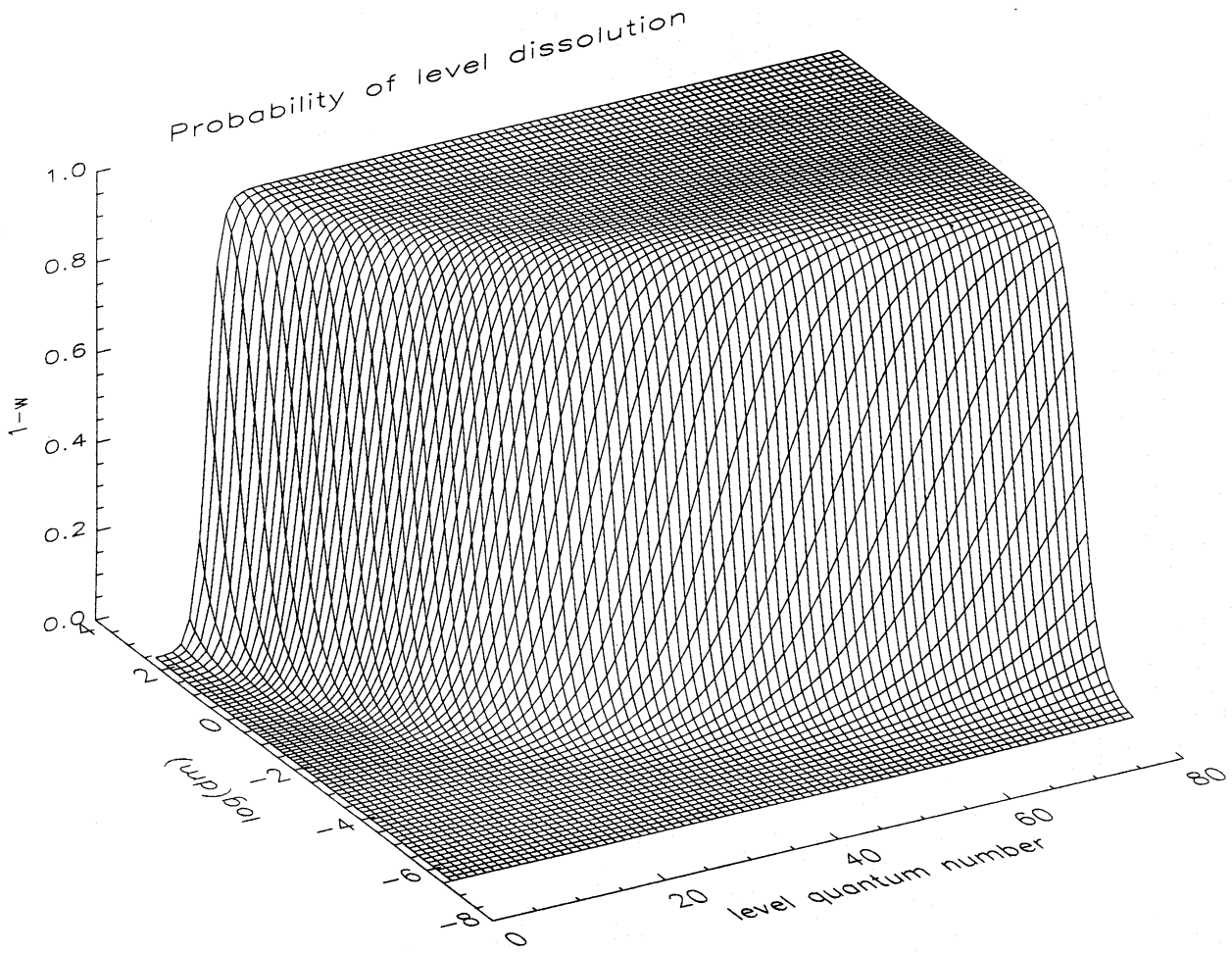

Fig. 1. Probability of level dissolution, defined as $1-w$, w being the occupation probability, as a function of the principal quantum number, and the depth in the atmosphere (expressed as a column mass in g/cm^2), for a representative pure-hydrogen model atmosphere with $T_{\rm eff}$= 20000 K, log g = 4 (model A of Sect. 4)

In the first term, the factor $df_{ij}/d\nu$ may be written to a good approximation as $f_{ij}\phi_{ij}(\nu)$ (see DAM), where f_{ij} is the usual oscillator strength, and $\phi_{ij}(\nu)$ the normalized absorption profile coefficient ($\int \phi_{ij}(\nu)d\nu = 1$). In the second term, we observe that the factor $1-w_j$ varies very slowly with j for large j (in fact, it approaches unity), and may be taken out of summation. We will therefore write for sufficiently large j

$$\sum_{j>i}(1-w_j)\frac{df_{ij}}{d\nu} \approx (1-w^*)\sum_{j>i}\frac{df_{ij}}{d\nu} \equiv [1-w^*(\nu)]\sigma_{i\kappa}(\nu), \tag{2.5}$$

where $\sigma_{i\kappa}(\nu)$ is the extrapolated photoionization cross–section. The latter equality follows from continuity of the line and continuum oscillator strength density (see, for instance, Fano & Cooper 1968), which was also used by DAM. The true absorption coefficient (2.4) may then be written as

$$\chi_i^{\rm abs}(\nu) = n_i\left[\sum_{j>i} w_j\sigma_{ij}(\nu) + \sigma_{i\kappa}^{\rm tot}(\nu)\right], \tag{2.6}$$

where

$$\sigma_{ij}(\nu) = \frac{\pi e^2}{mc}f_{ij}\phi_{ij}(\nu) \tag{2.7}$$

is the bound–bound cross–section, and

$$\sigma_{i\kappa}^{\rm tot} = D_i(\nu)\sigma_{i\kappa}(\nu), \tag{2.8}$$

where

$$D_i(\nu) = \begin{cases} 1, & \text{if } \nu \geq \nu_{i\kappa}; \\ \dfrac{1}{\sigma_{i\kappa}(\nu)}\displaystyle\sum_{j>i}(1-w_j)\frac{df_{ij}}{d\nu}, & \text{if } \nu < \nu_{i\kappa} \end{cases}; \tag{2.9}$$

here $\nu_{i\kappa}$ is the free atom ionization frequency.

In analogy with DAM we call $D_i(\nu)$ the *dissolved fraction*. However, their dissolved fraction is given by (see Eqs. 32 and 31 of DAM)

$$D_i^{\rm DAM}(\nu) = \frac{w_i - w_{n^*}}{w_i}, \quad n^* = \left(\frac{1}{i^2} - \frac{h\nu}{\chi_{ION}}\right)^{-1/2} \tag{2.10}$$

The effective quantum number n^* designates the highest state that can be reached from state i by the absorption of a photon

© European Southern Observatory • Provided by the NASA Astrophysics Data System

1994A&A...282..151H

of energy $h\nu$. As n^* defined by Eq. (2.10) need not be an integer, w_{n^*} is computed from an analytical expression for the occupation probability (see Appendix A).

Our formulation thus differs from DAM in two aspects:

i) The DAM form of $D(\nu)$ is based on heuristic arguments, while our formalism gives a prescription for calculating the dissolved fraction (although in practice the DAM form is probably a good approximation); and

ii) our expression does not contain the occupation probability of the lower level, w_i. This is because we use *conditional* probabilities, namely that *if* an atom in state i is undissolved, the probabilities of transition $i \rightarrow j$ to the undissolved and dissolved parts of the state j are equal to w_j and $1 - w_j$, respectively. It is this introduction of conditional probabilities that makes possible the generalization to NLTE conditions.

In contrast, DAM write $n_i = n_i^a + n_i^b$, and take the populations n_i^a and n_i^b be representative of the two possibilities. The populations n_i^a and n_i^b are in turn expressed through the probabilities w^a and w^b, which represent the *joint* probabilities that (a) state i *and* state j are both undissolved, and (b) state i is undissolved *and* state j is dissolved. The sum of probabilities w^a and w^b is therefore equal to w_i (< 1), so that in order to satisfy the above expression for populations one has to put $n_i^a = (w_j/w_i)n_i$ and $n_i^b = [(w_i - w_j)/w_i]n_i$. However, this means that these populations reflect the fact that state i may be dissolved, which is in conflict with the physical meaning of Eq. (2.4) or (2.6).

However, this difference is primarily conceptual and it is unlikely to be important in the present application, since the line merging to the series limit is important for spectral series with low lying starting levels (as, for instance, the Lyman and Balmer series of hydrogen), where the occupation probability is very close to unity anyway. For all practical applications, we will adopt for D_i the DAM form (2.10) with $w_i = 1$.

It remains to specify the spontaneous emission coefficient; in general the coefficient for stimulated emission is

$$\eta^{\rm stim}(\nu) = (c^2/2h\nu^3)\eta^{\rm spont}(\nu)I(\nu),$$

$I(\nu)$ being the specific intensity of radiation. The contribution of downward bound–bound transitions is given by

$$\sum_{j>i} \frac{h\nu_{ij}}{4\pi} n_j A_{ji} w_i,$$

where A_{ji} is the Einstein coefficient for spontaneous emission. Now the state j is the initial level, so the number of undissolved atoms in state j is correctly described by n_j, but we must include w_i, the probability that the final state is undissolved. The contribution of free–bound transitions is simply given by

$$(2h\nu^3/c^2)\exp(-h\nu/kT)n_\kappa(n_i/n_\kappa)^*\sigma_{i\kappa}(\nu)w_i,$$

which follows from the Einstein–Milne relations for the continuum. Because these relations are independent of the ionization limit the usual relations between the photoionization and recombination cross–sections remain valid.

Using the relation between the Einstein A coefficient and the oscillator strength, and the definition of the bound–bound cross–section, we may write for the emission coefficient at frequency ν due to all possible transitions ending at state i

$$\eta_i(\nu) = (2h\nu^3/c^2)w_i \left[\sum_{j>i} n_j(g_i/g_j)\sigma_{ij}(\nu) + n_i^* \exp(-h\nu/kT)\sigma_{i\kappa}^{\rm tot}(\nu)\right]. \tag{2.11}$$

Finally, we give the form of absorption coefficient corrected for stimulated emission,

$$\chi_i(\nu) = \sum_{j>i} \left[w_j n_i - w_i n_j(g_i/g_j)\right]\sigma_{ij}(\nu) + \left[n_i - w_i n_i^* \exp(-h\nu/kT)\right]\sigma_{i\kappa}^{\rm tot}(\nu). \tag{2.12}$$

2.3. Statistical equilibrium

Let us formulate the statistical equilibrium equation for state i. We stress again that since the population n_i represents the number density of atoms in undissolved state i, all transition probabilities $i \rightarrow j$ used in the rate equations should be understood as *conditional* probabilities, given the state i being undissolved.

2.3.1. Collisional rates

We can express formally the total rate of collisional transitions out of state i as

$$n_i \left[\sum_{j\neq i} w_j C_{ij} + \sum_{j\neq i}(1 - w_j)C_{ij} + C_{i\kappa}\right], \tag{2.13}$$

where the quantity C_{ij} in the first term is the collisional rate for the transition $i \rightarrow j$ to the unperturbed fraction of state j, while in the second term C_{ij} represents ionization into the dissolved fraction of this state. $C_{i\kappa}$ is the collisional ionization rate in the absence of level dissolution. The second term is logically combined with the normal rate to form the effective ionization rate coefficient

$$C_{i\kappa}^{\rm tot} = C_{i\kappa} + \sum_{j\neq i}(1 - w_j)C_{ij}. \tag{2.14}$$

Unlike the photoionization rate, which depend on the (a priori unknown) radiation field, the complete collisional ionization rate may be easily evaluated from Eq. (2.14).

The total number of collisional transitions *into* the state i is

$$w_i \left[\sum_{j\neq i} n_j C_{ji} + n_k C_{ki}^{\rm tot}\right], \tag{2.15}$$

because now state i is the final state of transitions $j \rightarrow i$, and therefore probability that it is not dissolved has to be taken into account. Obviously, the remaining fraction of transitions

© European Southern Observatory • Provided by the NASA Astrophysics Data System

1994A&A...282..151H

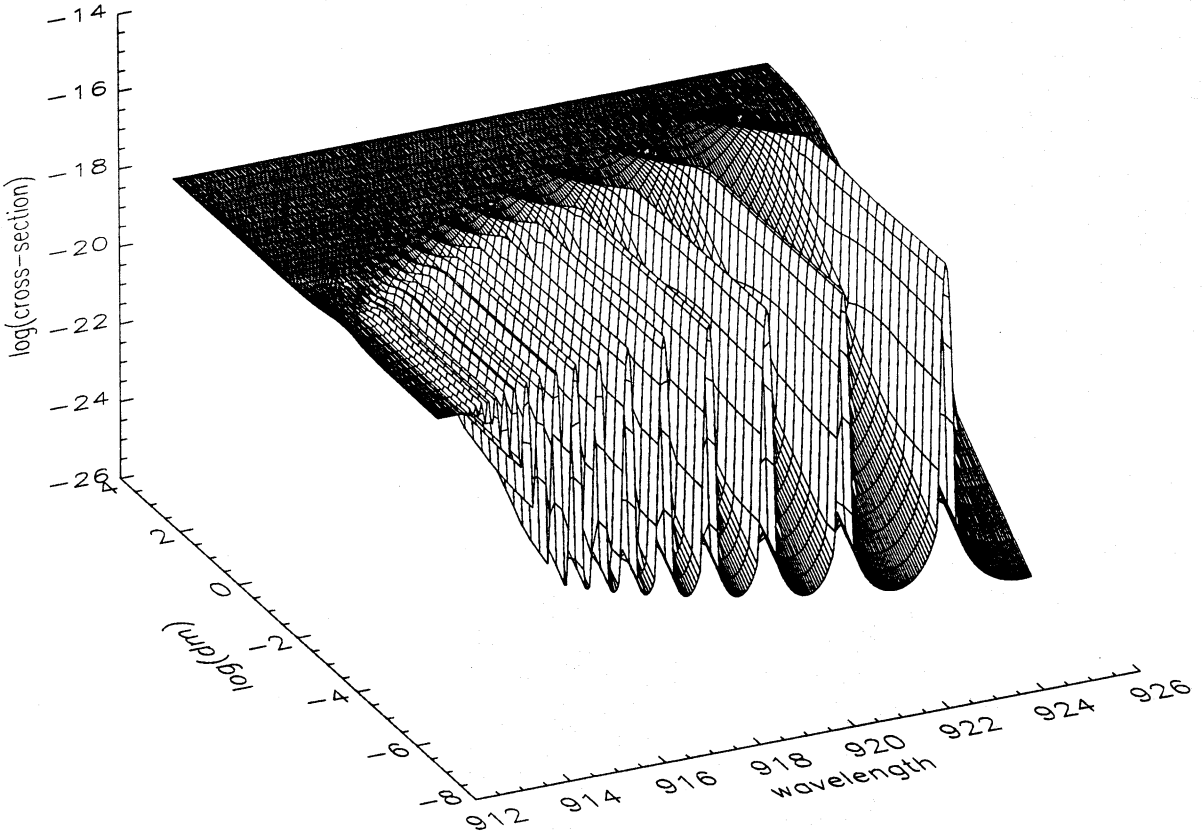

Fig. 2. Two-dimensional plot of the absorption cross-section (defined by Eq. 3.5) near the Lyman discontinuity for a pure-hydrogen model atmosphere with $T_{\rm eff}$= 20000 K, log g = 4 (model A of Sect. 4). The cross-section is plotted as a function of wavelength and depth in the atmosphere, analogous to Fig. 1

to the dissolved component of state i does not have to be dealt with explicitly, because these transitions are in fact collisions between ions and therefore do not contribute to the population of true, undissolved, atom in state i (recall the meaning of the population n_i).

From the detailed balance relation for the transition $i \leftrightarrow j$

$$n_i^* w_j C_{ij} = n_j^* w_i C_{ji}, \tag{2.16}$$

we obtain

$$\frac{C_{ji}}{C_{ij}} = \frac{n_i^*}{n_j^*}\frac{w_j}{w_i} = \frac{g_i}{g_j}\exp[(E_j - E_i)/kT], \tag{2.17}$$

where the occupation probabilities cancel out and one recovers the standard relation between upward and downward rates. This is consistent with our basic picture that the wavefunctions (and therefore energies and transition rates) remain unchanged.

Analogously, we find for the total collisional recombination rate

$$C_{\kappa i}^{\rm tot} = (n_i/n_\kappa)^* C_{i\kappa}^{\rm tot}. \tag{2.18}$$

2.3.2. Radiative rates

Analogously, the total rate of radiative transitions out of state i is given by

$$n_i \left[\sum_{j \neq i} w_j R_{ij} + \sum_{j \neq i} (1 - w_j) R_{ij} + R_{i\kappa} \right], \tag{2.19}$$

where R_{ij} in the first term is the radiative rate for the transition $i \rightarrow j$, given by

$$R_{ij} = \begin{cases} A_{ij} + B_{ij}\bar{J}_{ij}, & \text{if } i > j; \\ B_{ij}\bar{J}_{ij}, & \text{if } i < j; \end{cases} \tag{2.20}$$

here $\bar{J}_{ij} = \int J_\nu \phi_\nu d\nu$ is the frequency averaged mean intensity of radiation, and A and B are the usual Einstein coefficients.

Just as with the collisions, we write the total rate to the dissolved upper states as

$$\begin{aligned} \sum_j (1 - w_j) R_{ij} &= \sum_{j>i} \frac{\pi e^2}{mc}\frac{4\pi}{h\nu_{ij}} f_{ij}(1 - w_j) \int d\nu J_\nu \phi_{ij}(\nu) \\ &= \frac{\pi e^2}{mc}\frac{4\pi}{h\nu_{ij}} \int d\nu J_\nu \sum_{j>i} (1 - w_j) f_{ij} \phi_{ij}(\nu). \end{aligned} \tag{2.21}$$

© European Southern Observatory • Provided by the NASA Astrophysics Data System

1994A&A...282..151H

The summation in the second line is precisely the term $(1 - w^*)\sigma_{i\kappa}$ we have introduced for description of opacity – see Eq. (2.5). A contribution from the transitions with $j < i$ does not appear as this would correspond to the unphysical case of a transition from an undissolved upper state to a dissolved lower state. We may reasonably assume that $w_j \simeq 1$ for $j < i$, and therefore the contribution of all terms with $j < i$ is negligible. The total ionization rate from level i is then

$$R^{\rm tot}_{i\kappa} \equiv R_{i\kappa} + \sum_{j>i}(1 - w_j)R_{ij} = \int d\nu J_\nu \sigma^{\rm tot}_{i\kappa}(\nu), \qquad (2.22)$$

where $\sigma^{\rm tot}_{i\kappa}(\nu)$ is given by equation (2.8). This is a very desirable feature, because *the same* bound–free cross–section is used in the expressions for absorption and emission coefficient, as well as in the rate equations.

2.3.3. Complete rate equations

Using equations (2.13) – (2.22), the complete rate equation for state i is written

$$n_i \left[\sum_{j\neq i} w_j(C_{ij} + R_{ij}) + C^{\rm tot}_{i\kappa} + R^{\rm tot}_{i\kappa}\right] = w_i \left[\sum_{j\neq i} n_j(C_{ji} + R_{ji}) + (n_i/n_\kappa)^*(C^{\rm tot}_{i\kappa} + R^{\rm tot}_{i\kappa})\right]. \qquad (2.23)$$

3. Numerical treatment of the line-merging opacity

The opacity, as given by Eq. (2.12), is a very complicated function of frequency. We demonstrate this in Fig. 2, where we plot the total absorption coefficient near the Lyman discontinuity for a pure-hydrogen model atmosphere with $T_{\rm eff}$= 20000 K, log g = 4, as a function of the wavelength and the depth in the atmosphere. The latter reflects the dependence of the opacity on temperature and electron density.

An inspection of Fig. 2 reveals several important features. The opacity is a much smoother function of wavelength at large depths than near the surface. Deep in the atmosphere the density is high, and consequently lines are broad and merge to the continuum at relatively large distances below the threshold. In contrast, near the surface where the density is low, the individual lines are very narrow and merge to a continuum only for very high series members. These are well-known features; an approximate expression for the last visible line as a function of electron density is known as the Inglis-Teller formula (see Mihalas 1978). Our formalism is physically more refined than the simple Inglis–Teller formula, but the basic picture is similar.

In the present context, Fig. 2 makes clear the numerical problems encountered in a treatment of line merging. The obvious, direct approach of selecting a set of frequency points to reproduce the shape of opacity closely enough so that the frequency integrations needed to evaluate the relevant radiative and heating rates are accurate requires an enormous (therefore impractical) number of points. Indeed, one would have to resolve all the individual lines near the surface, as an improper choice of integration points would simulate spuriously broad lines and cause errors in the atmospheric structure. Numerical experiments confirm that the direct method is not only very time-consuming but also, and most importantly, offers no guarantee that an adopted choice of frequency points is indeed sufficient. Moreover, such an analysis would have to be repeated for different stellar classes.

A straightforward way of dealing with this complex structure is through *opacity distribution functions* (ODF), appropriately generalized to NLTE conditions. In this approach one resamples the discretized monochromatic opacity to obtain a monotonic function of frequency in each of the previously specified frequency regions. The corresponding frequency integrals are unchanged, but are calculated using substantially smaller numbers of integration points - see Fig. 3. For a review of the ODF method applied in LTE situations, see e.g. Carbon (1984).

This idea may be implemented in two different ways in which the line–merging opacity is treated as: 1) an extension of the corresponding continuum opacity; or 2) an individual "superline". We shall refer to these choices as the *continuum* and the *superline* approaches. Both variants offer advantages and suffer drawbacks. We have implemented them both, which has the very important benefit of allowing us to assess the overall internal accuracy of the statistical approach, because both variants differ not only in a different treatment of the line-merging opacity, but also in various physical assumptions which have to be made. As we show in Sect. 4 and 5, the results of both approaches are very close indeed, which gives additional credibility to our models. In the following, we shall describe both variants in more detail.

3.1. Line–merging opacity treated as an extension of continuum

We rewrite Eq. (2.12) as

$$\chi_i(\nu) = \chi^{\rm line}_i(\nu) + \chi^{\rm cont}_i(\nu), \qquad (3.1)$$

where

$$\chi^{\rm line}_i(\nu) = \sum_{j=i+1}^{NL} \left[w_j n_i - w_i n_j (g_i/g_j)\right] \sigma_{ij}(\nu), \qquad (3.2)$$

and

$$\chi^{\rm cont}_i(\nu) = \sum_{j=NL+1}^{N^*} \left[w_j n_i - w_i n_j (g_i/g_j)\right] \sigma_{ij}(\nu) + \left[n_i - w_i n^*_i \exp(-h\nu/kT)\right] \sigma^{\rm tot}_{i\kappa}(\nu). \qquad (3.3)$$

Here, the first NL levels and transitions between them are treated explicitly. All lines in $\chi^{\rm line}_i(\nu)$ are treated separately; every line has its own set of frequencies for the numerical evaluation of the corresponding integrals. Likewise, the statistical equilibrium equations are solved for levels $i = 1, \ldots, NL$ (the "NLTE levels" which we designate as "explicit levels"). The upper levels are assumed to be in LTE with respect to the ground

© European Southern Observatory • Provided by the NASA Astrophysics Data System

1994A&A...282..151H

state of the next ion. N^* is the highest level considered; it should be chosen sufficiently large to guarantee that the levels higher than N^* are essentially dissolved at all depths in the atmosphere. In the calculations described in Sect. 4 we have adopted $N^* = 80$, but also computed a test model with $N^* = 150$ as a check.

Treating the higher states in LTE and assuming that continuum transitions $i \rightarrow \kappa$ end in the ground state of the next ion, (the case of ionization to an excited state is a trivial generalization), Eq. (3.3) may be written as

$$\chi_i^{\rm cont}(\nu) = \left[n_i - w_i n_i^* \exp(-h\nu/kT)\right] \tilde{\sigma}_{i\kappa}(\nu), \qquad (3.4)$$

where

$$\tilde{\sigma}_{i\kappa}(\nu) = \sigma_{i\kappa}^{\rm tot}(\nu) + \sum_{j=NL+1}^{N^*} w_j \sigma_{ij}(\nu). \qquad (3.5)$$

In deriving Eqs. (3.4) and (3.5), we have replaced $\exp(-h\nu_{ij}/kT)$ (ν_{ij} being the frequency of the transition $i \rightarrow j$) by $\exp(-h\nu/kT)$). This assumption can be relaxed, but at the cost of introducing three different cross–sections for absorption (defined as in 3.5), stimulated and spontaneous emission. Although it would be easy to incorporate three different cross-sections represented by three different ODF's into the formalism, it would require a large amount of computer memory. In any event, the assumption of equal absorption and emission cross sections is quite accurate. Moreover, in deriving Eq. (3.4) we have ignored another difference between the cross-sections corresponding to the absorption and emission. In fact, Eq.(3.4) should be written as

$$\chi_i^{\rm cont}(\nu) = n_i \tilde{\sigma}_{i\kappa}^{\rm abs}(\nu) - w_i n_i^* \exp(-h\nu/kT) \tilde{\sigma}_{i\kappa}^{\rm em}(\nu), \quad (3.4a)$$

where $\tilde{\sigma}_{i\kappa}^{\rm abs}(\nu) = \tilde{\sigma}_{i\kappa}(\nu)$ as given by Eq. (3.5), while

$$\tilde{\sigma}_{i\kappa}^{\rm em}(\nu) = \sigma_{i\kappa}^{\rm tot}(\nu) + \sum_{j=NL+1}^{N^*} (w_j/w_i)\sigma_{ij}(\nu). \qquad (3.5a)$$

Replacing $\tilde{\sigma}_{i\kappa}^{\rm em}(\nu)$ by $\tilde{\sigma}_{i\kappa}(\nu)$ is justified because the line merging opacity is important for transitions from low-lying states ($n = 1$ or 2), for which the corresponding occupation probability w_i is very close to unity.

The last step is to resample the cross–section (3.5) on the frequency interval $\nu_{i,NL} < \nu < \nu_{i\kappa}$ (i.e. between the last explicit line of the spectral series originating at level i and the true threshold) to obtain a monotonically decreasing function of frequency, $\tilde{\sigma}_{i\kappa}^{\rm ODF}$ - see Fig. 3. The complete cross-section is then

$$\sigma_{i\kappa}^{\rm ODF}(\nu) = \begin{cases} \sigma_{i\kappa}(\nu), & \text{if } \nu \geq \nu_{i\kappa}; \\ \tilde{\sigma}_{i\kappa}^{\rm ODF}, & \text{if } \nu < \nu_{i\kappa} \end{cases}. \qquad (3.6)$$

In this formalism, the contribution of high series members to the opacity/emissivity and to the statistical equilibrium (radiative rates) is represented simply by replacing $\sigma_{i\kappa}^{\rm tot}(\nu)$ by $\sigma_{i\kappa}^{\rm ODF}(\nu)$ in the expressions for absorption coefficient, emission coefficient, and the radiative rates, Eqs. (2.12), (2.11), (2.22), respectively.

3.2. *Line–merging opacity treated as a superline*

Another way of treating the line-merging opacity is to form a separate "supermultiplet", or a "superline" rather than to include it in the continuum. To this end, we have to introduce several concepts. A similar approach was also applied by Anderson (1989), who used this idea to group the energy levels of the iron-peak elements.

First, we group all levels $j = NL + 1, \ldots, N^*$ to one "superlevel", (or *merged level*) which will be denoted as J. The basic physical assumption is that all real levels j forming the superlevel J have a common NLTE departure coefficient, or, in other words, all components j are in LTE with respect to each other. Their common b–factor may, however, be different from unity. The population of level J is defined as

$$n_J = \sum_{j=NL+1}^{N^*} n_j. \qquad (3.7)$$

Defining the statistical weight as

$$g_J = \sum_{j=NL+1}^{N^*} w_j g_j \exp(E_j/kT), \qquad (3.8)$$

where E_j is the ionization energy from level j (i.e. the ionization energy from the ground state minus the excitation energy of level j) and formally setting

$$w_J = 1, \qquad (3.9)$$

because the occupation probabilities are already considered in the statistical weight, Eq. (3.8), we may write the Saha–Boltmann factor as

$$\phi_J(T) = CT^{-3/2} g_J/(2g_k),$$

This correspond formally to setting the excitation energy $E_J = \chi_{\rm ION}$. The LTE population of level J is now given by the usual expression,

$$n_J^* = n_e n_\kappa \phi_J(T),$$

where the constant $C = 2.07016 \times 10^{-16}$, and κ denotes the ground state of the next ion.

The opacity from all transitions starting from level i, Eq. (2.12), may now be written as

$$\chi_i(\nu) = \chi_i^{\rm line}(\nu) + \chi_i^{\rm merge}(\nu) + \chi_i^{\rm cont}(\nu), \qquad (3.10)$$

where $\chi_i^{\rm line}$ is given by Eq. (3.2), but $\chi_i^{\rm cont}$ contains only the second term of the r.h.s of Eq. (3.3), and is given by

$$\chi_i^{\rm cont}(\nu) = \left[n_i - w_i n_i^* \exp(-h\nu/kT)\right] \sigma_{i\kappa}^{\rm tot}(\nu). \qquad (3.11)$$

The remaining contribution from transitions to all components of the merged level, i.e. one superline, is given by

$$\chi_i^{\rm merge}(\nu) = \left[n_i - n_J \frac{g_i}{g_J}\right] \sigma_{iJ}(\nu), \qquad (3.12)$$

© European Southern Observatory • Provided by the NASA Astrophysics Data System

1994A&A...282..151H

where the "absorption profile" of the superline, $\sigma_{iJ}(\nu)$, is given by

$$\sigma_{iJ}(\nu) = \sum_{j=NL+1}^{N^*} w_j \sigma_{ij}(\nu). \tag{3.13}$$

Again, the stimulated emission term as given by the second term on the r.h.s. of Eq. (3.10) is an approximation, based on the expression

$$\sum_{j=NL+1}^{N^*} w_j \exp(-h\nu_{ij}/kT)\sigma_{ij}(\nu) \simeq \exp(-h\nu/kT) \sum_{j=NL+1}^{N^*} w_j \sigma_{ij}(\nu). \tag{3.14}$$

In the same approximation, the emission coefficient is

$$\eta_i^{\rm merge}(\nu) = \frac{2h\nu^3}{c^2} w_i n_J \frac{g_i}{g_J} \sigma_{iJ}(\nu). \tag{3.15}$$

Equations (3.12) and (3.15) are identical to the expressions for the opacity and emissivity of a normal line, replacing j (indicating a single level) by J (indicating a merged level). In fact, an analogous approximation is often made for spectroscopic multiplets, replacing the individual energy eigenstates by an averaged level, and the individual components of a multiplet by a single line. In the present case, there are many components forming the supermultiplet and, moreover, the level dissolution is taken into account which means that a different number of lines effectively contribute to the supermultiplet at different depths in the atmosphere. Also, unlike genuine multiplets, where a single line representing the multiplet is assumed to have the same absorption profile (for instance, a Voigt profile), the present case is more complicated. However, we may construct a resampled opacity to obtain an ODF, which is then represented by a relatively small number of frequency points. Formally, this is represented by replacing everywhere

$$\sigma_{iJ}(\nu) \rightarrow \sigma_{iJ}^{\rm ODF}(\nu).$$

Level J thus formally behaves as a normal level, and all usual expressions for absorption and emission coefficients, and radiative rates are unchanged if we substitute $\sigma_{iJ}^{\rm ODF}(\nu)$ for an ordinary absorption profile $\sigma_{ij}(\nu)$. To complete the formalism, we need explicit expressions for the photoionization cross section from the merged level, and for collisional rates between the ordinary (explicit) levels and the merged level, which are respectively

$$\sigma_{J\kappa}(\nu) = \frac{1}{g_J} \sum_{j=NL+1}^{N^*} w_j g_j \exp(E_j/kT)\sigma_{j\kappa}(\nu), \tag{3.16}$$

and

$$C_{J\kappa} = \frac{1}{g_J} \sum_{j=NL+1}^{N^*} w_j g_j \exp(E_j/kT) C_{j\kappa}, \tag{3.17}$$

Finally, the collisional excitation rates are given by

$$C_{iJ} = \sum_{j=NL+1}^{N^*} C_{ij}. \tag{3.18}$$

Downward collisional rates are given by the standard expressions.

3.3. Comparison of the continuum and the line approach

The line approach is more elegant, allows greater flexibility, but is slightly more complicated to code. On the other hand, the continuum treatment can be implemented by a very straightforward modification of any existing model stellar atmosphere code. In addition to supplying routines for the evaluation of the resampled cross-section $\sigma_{i\kappa}^{\rm ODF}(\nu)$, the only modification to the program is that of allowing the continuum cross-sections be generally depth-dependent. Obviously, another modification is necessary to include the occupation probabilities, but this is common to both treatments.

An essential disadvantage of the continuum approach, however, is its inflexibility concerning the treatment of frequency points. All the integration points representing the ODF part of the continuum cross-section (of the order of 10 to 20 points per ODF) have to be treated on the same footing as the integration points for the corresponding continuum. If one uses a method based on complete linearization, as we do, all frequency points in the ODF's have to be the "explicit" frequency points, i.e. those in which the radiation intensities are linearized. Since for complete linearization the computer time scales roughly as the cube of the number of unknowns, the increase of the computer time due to ODF's may be appreciable (although obviously still by orders of magnitude smaller than by treating the line-merging opacity directly).

Another disadvantage is that if we choose to perform a set of equivalent-two-level-atom (ETA) procedures between two successive linearizations (which in some cases may speed up convergence or even prevent divergences; for details, see Hubeny 1988), for a continuum which is supplemented by an ODF (a typical example being the hydrogen Lyman continuum supplemented by the Lyman lines ODF), the ODF frequency points have to be included in the ETA procedure, which may take excessive computer time.

On the other hand, the superline approach avoids the above problems completely. The superlines may be treated as "fixed-option" transitions (see Hubeny 1988), which means that they are treated essentially exactly, but their radiative rates are not linearized. As discussed by Hubeny & Lanz (1992a), treating many transitions in the fixed option increases somewhat the number of iterations but the reduction of computer time per iteration may be enormous. Also, by treating the ODF's as fixed transitions we can afford to represent the ODF by more frequency points, which obviously increases the internal accuracy of the models. We have performed many tests and verified that treating the ODF's as explicit or fixed transitions always gives the same atmospheric structure (for instance, the temperature

© European Southern Observatory • Provided by the NASA Astrophysics Data System

1994A&A...282..151H

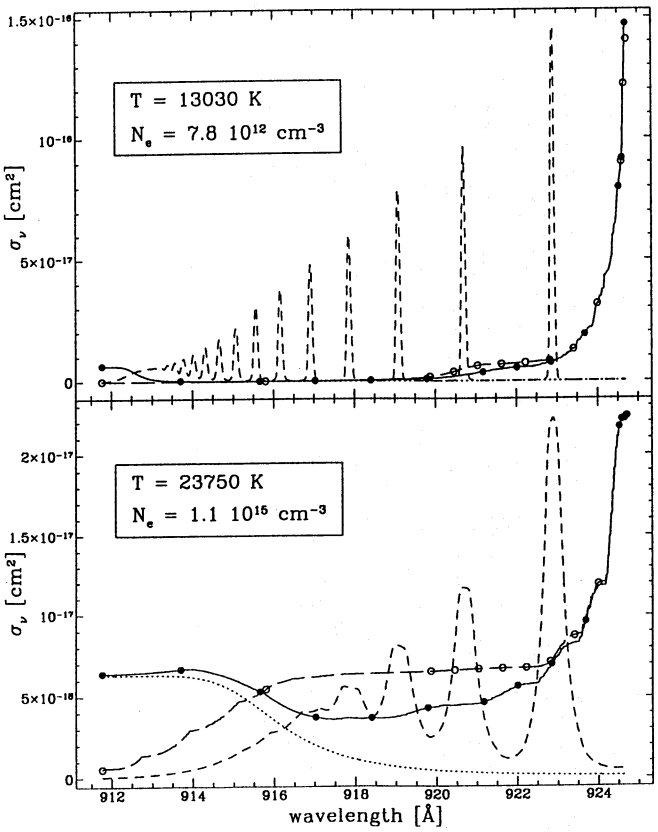

Fig. 3. Exact opacity due to Lyman lines (short dashes), and pseudocontinuum (dotted line), together with its representation in terms of opacity distribution functions. The long-dashed line is the "continuum" ODF, obtained by resampling the total, lines + pseudocontinuum, cross-section (Eq. 3.5); the full line is the representation in the "line" ODF formalism (Sect. 3.2. - Eqs. 3.13 and 3.10), where only the true line opacity (short-dashed line) is resampled, and the pseudocontinuum part is then added. The circles indicate the frequency quadrature points used to represent the corresponding ODF's in the model calculations; filled circles – the line ODF, and empty circles – the continuum ODF. The cross-sections and ODF's are plotted for two depths in same model atmosphere as in Figs. 1 and 2, $T_{\rm eff}$= 20000 K, log g = 4 (model A of Sect. 4). Upper panel: the region of temperature minimum (cf Fig. 4). Lower panel: the region of formation of the far-UV continuum. The values of temperature and electron density are indicated in the upper left corner of the panels

difference was found to be less than 0.1 K everywhere in the atmosphere for all test calculations).

Very recently, we have developed a new method which allows us to linearize even the "fixed rates", in which the only quantity held fixed during the subsequent linearization step is an approximate lambda operator. The convergence rate is much higher than with using the traditional formulation of the fixed-option transitions. This method is therefore a hybrid combining complete linearization and the class of modern methods called accelerated lambda iteration (ALI – for a preliminary account see Hubeny & Lanz 1992b), and will be described fully in a forthcoming paper. Using this method, the advantages of the superline treatment of line merging is quite obvious. Finally, an important advantage of the superline treatment is the ease with which it can be generalized to treat line overlap, such as that between hydrogen and ionized helium. We shall consider this problem in a future paper.

The basic physical difference between the continuum and the line treatment of line merging is relatively subtle. As follows from a close inspection of Eqs. (3.3) and (3.11), the continuum-option ODF contains the contributions from both the "pseudo-continuum" (i.e. transitions from level i to dissolved states included in $\sigma_{i\kappa}^{\rm tot}(\nu)$) as well as from the genuine lines. In contrast, the superline-option ODF contains only the latter contribution, and the "pseudocontinuum" contribution has to be treated separately, namely as a extension of the true continuum. Since the internal cross-section to be resampled is different in these two approaches, the corresponding ODF is also different.

In using the ODF approach, one is free to choose the exact position of the peak of the ODF. A sensible strategy is to place it near the frequency where the original opacity has its maximum. In both cases, the position of the peak is chosen to lie between the last explicit line and the next higher line already incorporated to the ODF (for instance, if we consider 8 lowest levels of hydrogen as explicit, then the peak of the Lyman-line ODF is located between lines 1-8 and 1-9; and similarly for the Balmer ODF). The opacity then decreases with decreasing wavelength, and reaches a minimum just longward of the threshold. In the superline option, since the pseudocontinuum is treated directly, the total opacity (ODF + pseudocontinuum) first decreases with decreasing wavelength and then starts to increase due to the increasing opacity in the pseudocontinuum. This behavior is illustrated in Fig. 3.

In addition to all the advantages of the superline-option ODF discussed above, we feel that also the shape of total opacity better reflects the original opacity. In any case, the difference in model structure obtained with the two approaches provides us with a measure of the internal accuracy of the ODF approach. We shall return to this point in Sect. 5.

Finally, we would like to stress the following point. We are using the notion of ODF, which was traditionally used in the context of LTE. The basic differences between the NLTE and LTE implementations of the idea of ODF are: i) in LTE, all lines of all chemical species in a given frequency interval are grouped to one ODF; ii) here, a separate ODF is constructed not only for individual atoms and ions, but also for the individual groups of lines such as the Lyman and Balmer series; iii) NLTE ODF's are used not only in the radiative and the hydrostatic equilibrium equations (as in LTE), but also in the statistical equilibrium, through the radiative rates to and from the superlevels, as well as through the contributions of superlevels to the radiative rates of the transitions which overlap them.

The idea of NLTE ODF is not limited to the treatment of transitions between the explicit states and higher, partly dissolved, states, as described here. The same idea may be applied to any groups of levels, which is particularly useful for species with a complicated energy level structure, in particular the iron group elements. In this context, a similar approach was already used by Anderson (1989) and Dreizler & Werner (1992) for a

© European Southern Observatory • Provided by the NASA Astrophysics Data System

1994A&A...282..151H

Table 1. Characteristics of the model stellar atmospheres: number of NLTE levels and frequencies (total and linearized), and type of line profiles.

Model	NLTE levels	Frequencies tot.	lin.	Profiles
A	$8+1^a$	362	160	Stark
B	8	362	203	Stark
S	8	291	174	Stark
N	8	228	111	Doppler
A′	$8+1^a$	446	202	Stark
X	$12+1^b$	540	203	Stark

[a] Merged level, $n = 9,\ldots, 80$
[b] Merged level, $n = 13,\ldots, 80$

statistical treatment of NLTE line blanketing due to various ions of iron. Our approach, the first results, and a comparison to the above mentioned studies, were briefly presented in Hubeny & Lanz (1992b). We shall defer a more detailed discussion of our general NLTE ODF approach to a forthcoming paper.

4. Illustrative examples and discussion

To demonstrate the importance of a correct treatment of occupation probabilities and of the line merging near the series limits, we assume for simplicity a pure hydrogen atmosphere. We have selected two effective temperatures, $T_{\rm eff}$= 20000 and 35000 K, and log g = 4, to assess the importance of these phenomena for main sequence early B and early O stars. We are also studying these effects in early A stars and white dwarfs, for which the effects are obviously largest; the results will be presented elsewhere.

In all models, departures from LTE are allowed for 8 lowest (explicit) levels; the higher levels up to n=80 are populated according to Eq. (2.1), ie. LTE with occupation probabilities. All lines between the explicit levels are included. The calculations were carried out using the model atmosphere code TLUSTY (Hubeny 1988), upgraded by various acceleration schemes as described by Hubeny & Lanz (1992a), and modified to include occupation probabilities and line merging opacity.

For both effective temperatures, we have calculated four models differing in the treatment of the Lyman and Balmer lines - see Table 1. Model N represents a "classical" model, i.e. with no opacity due to high members of the Lyman and Balmer series. The continuum edges are treated as sharp, as in most previous studies, and Doppler profiles are assumed for all lines. Model S differs from model N only in that Stark profiles are taken for the Lyman and Balmer lines. As in both cases the profiles are taken as depth-dependent, the frequency integration weights are depth-dependent in order to guarantee the exact normalization of the profile function. We note that the comparison between models N and S is analogous to the study of Rauch & Werner (1988).

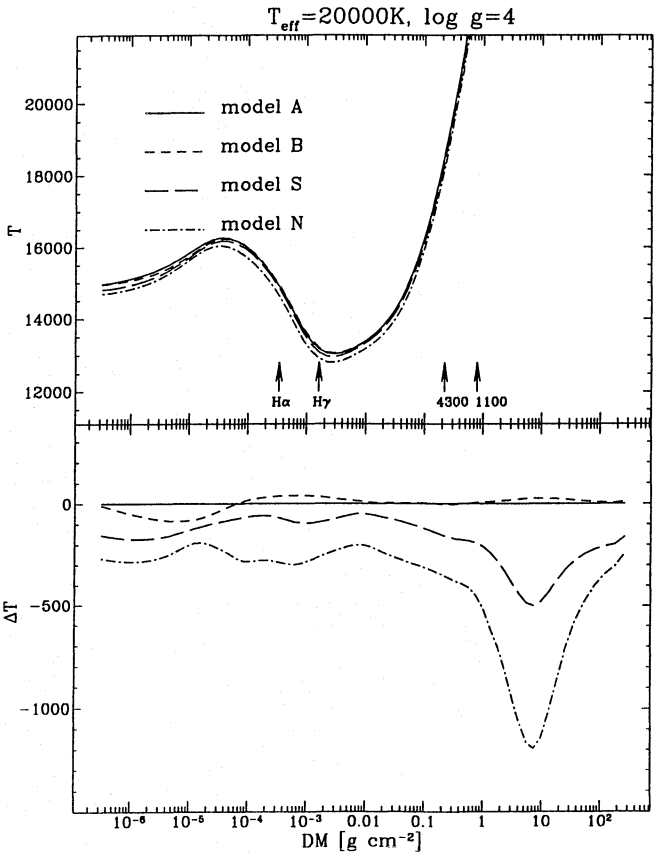

Fig. 4. Plot of the temperature (upper panel), and the temperature differences with respect to model A (lower panel) for the models A, B, S, N, for $T_{\rm eff}$= 20000 K, log g = 4. The abscissa is the depth in the atmosphere expressed as a column mass in g/cm^2

Models A and B represent the "exact" model as far as the treatment of level dissolution and line merging is concerned. Model A uses occupation probabilities and the line ODF to treat the line merging, while model B uses the continuum approach. As discussed in Sect. 3c, the comparison of A and B gives information about the internal accuracy of our modeling procedure.

In the model construction, instead of the exact Stark+Doppler broadening functions we have used the approximation described in Appendix B. Tests show that for high members of the series the accuracy is of the order of 1 to 2 %, while for lower lines the errors are on the order of several per cent. Once the model atmosphere is constructed, detailed line profiles are calculated using the synthetic spectrum program SYNSPEC (Hubeny, unpublished), where the exact line broadening functions are used.

In Fig. 4 the run of temperature versus the column mass is shown for $T_{\rm eff}$=20000 K together with the differences of temperature from model A. Arrows indicate the depths of formation (defined as the monochromatic optical depth equal to 2/3) of four spectral features: the centers of Hα and Hγ, the continuum in the vicinity of Hγ, and the short–wavelength side of the Balmer continuum at 1100 Å.

© European Southern Observatory • Provided by the NASA Astrophysics Data System

1994A&A...282..151H

Several interesting conclusions may be drawn. First, the differences in the temperature structure between the model N (classical) and A (exact) are important. The classical model is significantly cooler everywhere – in deep layers by more than 1000 K, and in the region of formation of the optical spectrum by 300 to 400 K. The higher temperature in model A is explained by the classical backwarming effect: the flux blocked by the broad hydrogen line wings (mainly of the Lyman series) and by the pseudocontinuum region near the Lyman limit has to be redistributed in the continua, thus heating the deep layers.

Second, the difference between models A and B is very small throughout most of the atmosphere – of the order of 40 K or less at the line and continuum forming layers and at most 80 K at the surface. However, since the heat capacity of the surface layers is very small, they are extremely sensitive to every detail of the computational procedure. But in reality, these differences are of little significance, for they do not significantly influence any observable spectral feature and, moreover, the surface would be dominated by metal line blanketing. Nevertheless, the small difference in the temperature structure even in the surface layers indicates that our statistical procedures do indeed provide a reliable description of the line merging problem.

Third, model S is about half way between A and N. This indicates that roughly half of the backwarming is caused by the wings of the lines up to $n \rightarrow 8$ (n = 1 or 2), and the other half by the cumulative effect of higher series members and the corresponding pseudocontinua. This conclusion is different from that of Rauch & Werner (1988), who concluded that the differences in the temperature structure between the N-type and S-type models is negligible. However, they studied much hotter stars, where the Lyman and Balmer line wings are narrower, and therefore their influence much weaker. We return to this point below.

From the standpoint of spectroscopic diagnostics, the effect of differences in atmospheric structure on the emergent line profiles is crucial. Therefore, we present a comparison of profiles for the Hα line (Fig. 5), Hγ (Fig. 6), and the short-wavelength portion of the Balmer continuum containing all Lyman lines (Fig. 7). All the synthetic spectra are generated using the *exact* line broadening functions (Vidal et al. (1973) for the first four members of the Lyman and Balmer series; Butler (private communication) for higher Balmer lines to H_{10}).

Neglecting the Lyman and Balmer line merging yields a difference of about 4 % in the relative profile of Hα (at about 0.7 Å from the line center); and about 3 % for Hγ, which is important and easily measurable. Also, the difference between models S and N calculated with Stark and Doppler profiles reaches about 2 % . Therefore, the interpretation of modern high–quality spectrophotometric data require models of corresponding quality, namely A– or B–type models. Differences between models A and B are less than 0.3 %, which can be viewed as the upper limit of the absolute accuracy of the present modeling techniques. In real stellar atmospheres there will certainly be other phenomena contributing to line profiles at a higher level, but the important conclusion of the present study is that potentially serious errors on the order of several per cent resulting from incorrect treatment of higher Lyman and Balmer lines are now well under control.

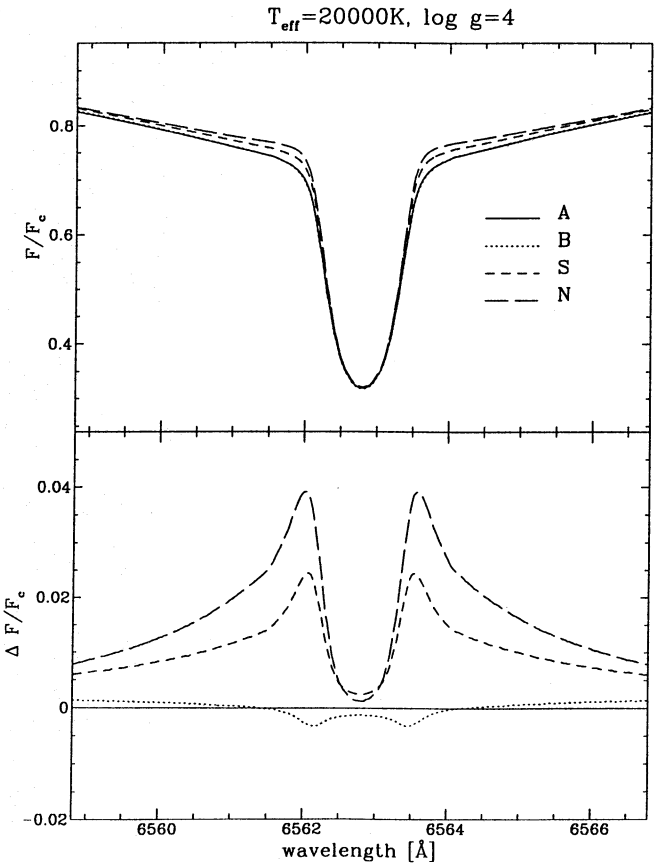

Fig. 5. Hα relative profiles (upper panel) and the difference of the relative profiles (lower panel) for the four models displayed in Fig. 4. The relative profile is defined as the computed absolute flux divided by the computed continuum flux

As may be deduced from Fig. 4, the short–wavelength portion of the Balmer continuum should be influenced most, because it is formed where the temperature difference is largest. This is dramatically demonstrated in Fig. 7, which shows relative errors up to 15% in the continuum and 35 % in the near line wings! The internal accuracy of the modeling procedure is verified as differences between A and B are less than 1 per cent.

Figures 8–11 show analogous comparisons for the models at $T_{\rm eff}$=35000 K. The temperature profile (Fig. 8) is similar to that of the $T_{\rm eff}$=20000 K models. Differences between models A and N are now smaller, as expected from the much narrower Lyman and Balmer lines. In fact, these lines are so narrow (see also Fig. 11) that the backwarming in the continuum–forming and deeper layers is now merely 200 K, while the maximum difference occurs in the line–forming regions (about 700 K). This indicates that that the primary effect responsible for the temperature differences is the indirect non-LTE effect, first discussed by Auer & Mihalas (1969; see also Mihalas 1978): the Balmer lines provide an efficient channel for populating the n = 2 level, thus enhancing the heating in the Balmer continuum. In the

© European Southern Observatory • Provided by the NASA Astrophysics Data System

1994A&A...282..151H

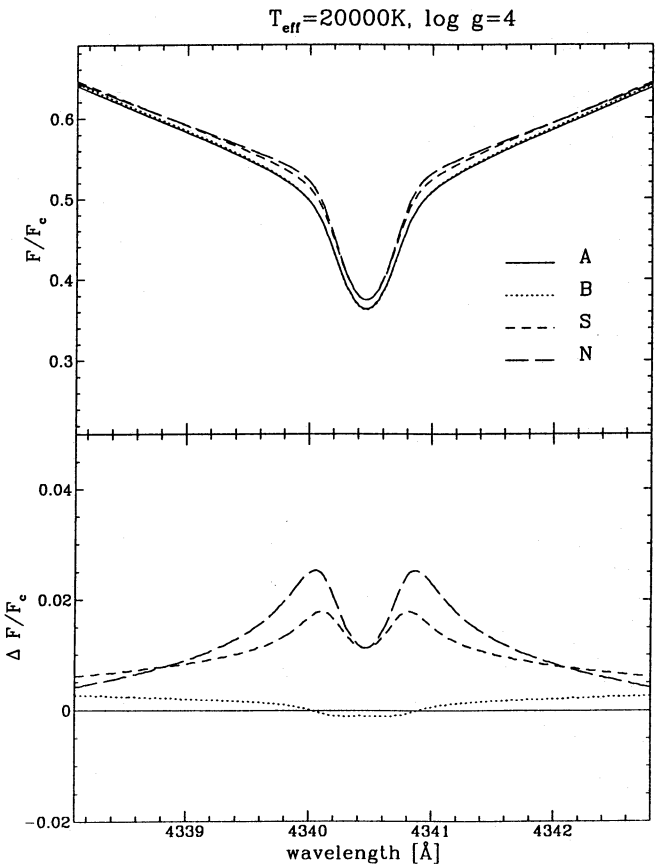

Fig. 6. The same as in Fig. 5, but for Hγ

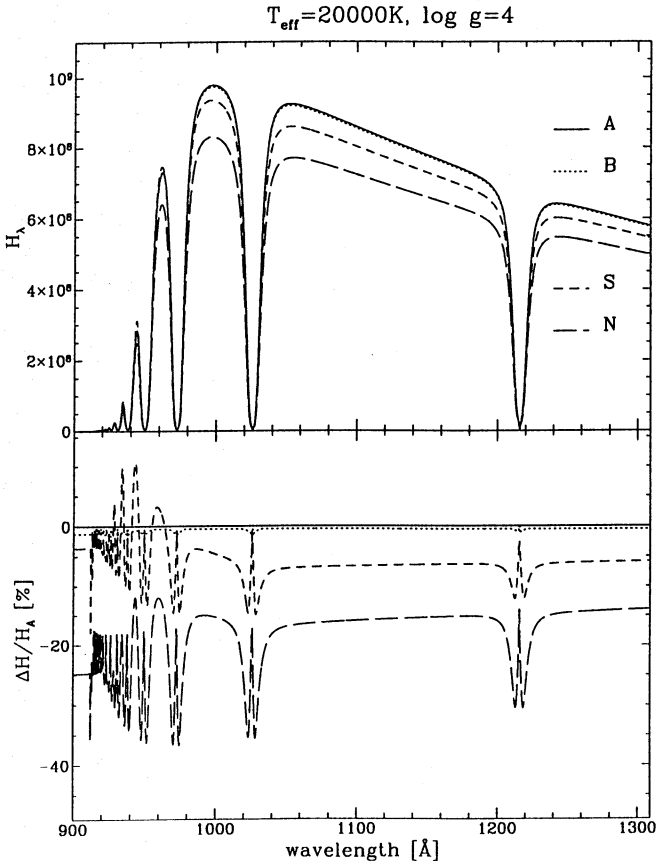

Fig. 7. The computed absolute flux in the far-UV region, including all Lyman lines, for the four models displayed in Figs. 4 to 6. The differences (lower panel) are expressed in per cent, $\Delta H = 100\,(H - H_A)/H_A$

present context, the broader and more numerous lines (model A as opposed to model N) enhance this heating effect.

The differences between models N and S (Doppler versus Stark profiles) are now rather small (around 200 K), in agreement with the results of Rauch & Werner (1988). Again, internal accuracy of the models is high; the temperature differences between models A and B are less than 50 K in the line– and continuum–forming regions, and reach about 100 K in the surface layers.

A comparison of the Hα and Hγ profiles is quite analogous to the case of 20000 K model. The differences between models A and N are of similar magnitude as before, while the differences between N and S are generally smaller. The comparison of the short–wavelength portion of the Balmer continuum and Lyman lines reveals very small differences – about 2 per cent, in a sharp contrast to the cooler models (cf Fig. 7).

5. Internal accuracy

Two questions remain remain regarding the internal consistency of our models. The first concerns the extent to which the models are sensitive to the details of the treatment of explicit lines (namely the number of frequency points, the type of frequency quadrature, and the treatment of the background continuum). The second concerns the sensitivity of the models to the partitioning of levels into "explicit" and "higher" classes. All models discussed in this section are at $T_{\rm eff}$= 20000 K in view of their higher sensitivity to the treatment of hydrogen lines.

5.1. Constant versus frequency-dependent background opacity

All models considered above were calculated with the usual assumption that the line opacity is symmetric about the line center and that the background opacity is that at line center. The lines are therefore represented by half of the total profile. Frequency points and weights were calculated using a series of 3-point Simpson integrations with subsequent intervals doubled in size away from line center. Lα to Lγ were each represented by 15 frequency points between 0 and 254 fiducial Doppler widths from the center (the fiducial Doppler width corresponds to $T = 0.75T_{\rm eff}$), Lδ by 13 points extending to 128 Doppler widths, the lines $1 \rightarrow 6$ and $1 \rightarrow 7$ by 11 points extending to 62 Doppler widths, and the $1 \rightarrow 8$ line by 11 points extending to 42 Doppler widths. Each Balmer line is represented by 11 points extending to 62 Doppler widths.

The Balmer lines do not present any significant problems. Since the background continuum is very flat, the above representation should be quite accurate. We have calculated a test model with full profiles and exact (frequency-dependent) back-

© European Southern Observatory • Provided by the NASA Astrophysics Data System

1994A&A...282..151H

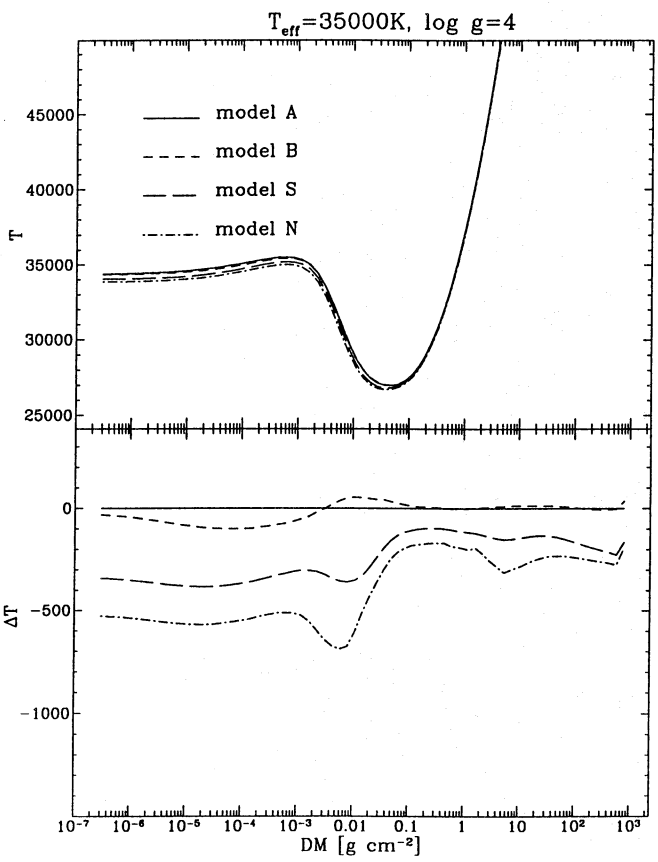

Fig. 8. An analogous plot as in Fig. 4, but for $T_{\rm eff}$= 35000 K, log g = 4

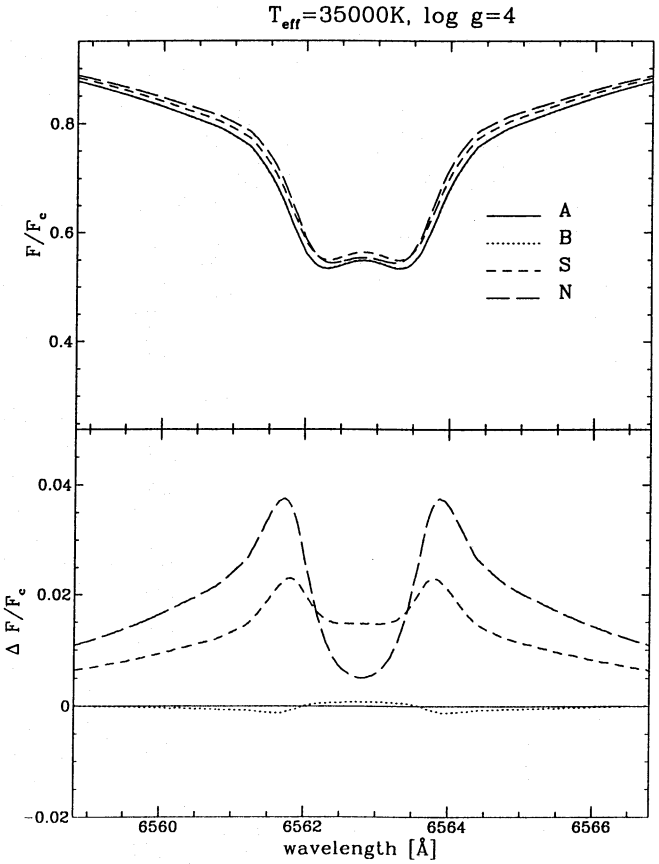

Fig. 9. An analogous plot as in Fig. 5, but for $T_{\rm eff}$= 35000 K, log g = 4

ground opacity for all Balmer lines, and have indeed found that the resulting differences were at most a few K.

To study errors resulting from the approximate treatment of the Lyman lines, we have calculated another model – A′ – in which all Lyman lines are represented by full profiles, with the frequency points placed symmetrically about line center; the number of points is now doubled. From Fig. 12 we see that the temperature differences between the $T_{\rm eff}$= 20000 K models are rather small – 50 K or less – in the line and continuum forming layers, and increase to about 300 K at depth. The corresponding differences in the Hγ profile, displayed in Fig. 13, are very small - of the order of 0.1 %. Thus, even for the Lyman lines, the half profile is an excellent approximation. This conclusion is very important because decreasing the number of frequency points in the Lyman lines leads to considerable savings of computer time.

5.2. *Dependence on the number of explicit levels*

Another crucial test of the reliability of our method is the comparison of models calculated with different number of explicit levels. Taking the superlevel and superline description, the sensitivity to the number of explicit levels should be very small, as *all* levels higher than the last explicit level are included into the corresponding superlevel, and *all* the opacity due to the higher lines is treated within the corresponding superline. Obviously, we cannot expect a complete agreement, because: i) the superline treatment assumes that all levels forming a superlevel share the common b-factor, while in reality these may vary, particularly if we extend the superlevel levels down to relatively low quantum number; ii) the notion of a superline is an inherently approximate description of the line merging opacity. Therefore different partitionings of the total line opacity into an "exact" (explicit) part and an ODF part may give different results.

To study this phenomenon, we have calculated a model, denoted X, where the number of explicit levels was increased from 8 to 12, and the remaining levels are combined into the superlevel. Figure 14 displays the differences in the temperature structure between models A, B, and X. The differences throughout most of the atmosphere are again very small, within 50 K, rising to about 150 K in the surface layers. That model X is actually closer to B than to A may be easily explained by the fact that A suppresses slightly the low opacity part of the Lyman line ODF (see Fig. 3) while in X this low-opacity part is now considered explicitly, in closer correspondence to B, in which the low-opacity part is never suppressed. Corresponding differences in the Hγ profile are plotted in Fig. 15. Again, the differences are well within 0.4 %, a value quite consistent with our absolute accuracy limit discussed in Sect. 4. These results demonstrate that the statistical method is indeed capable of providing a robust and reliable method of calculating model

© European Southern Observatory • Provided by the NASA Astrophysics Data System

1994A&A...282..151H

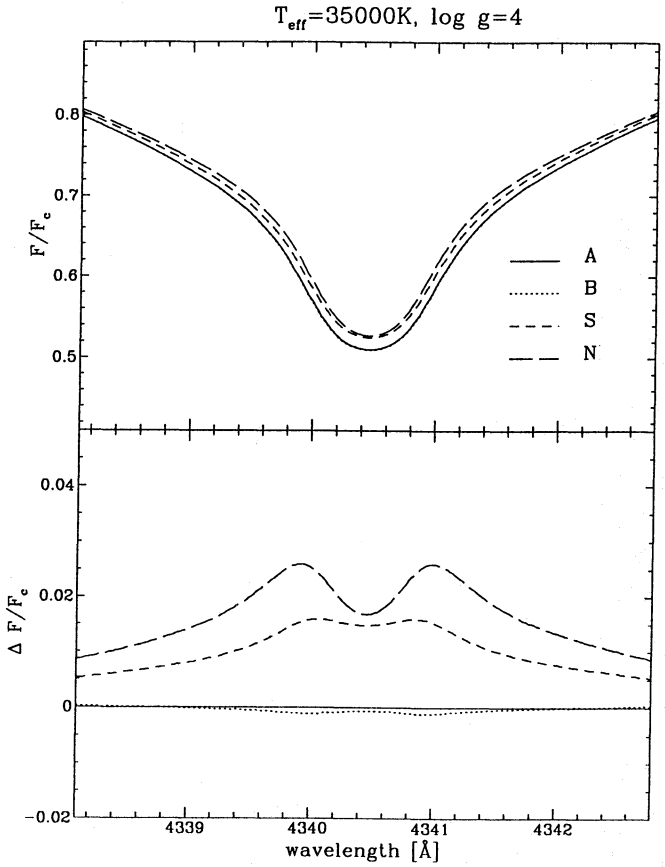

Fig. 10. An analogous plot as in Fig. 6, but for $T_{\rm eff}$= 35000 K, log g = 4

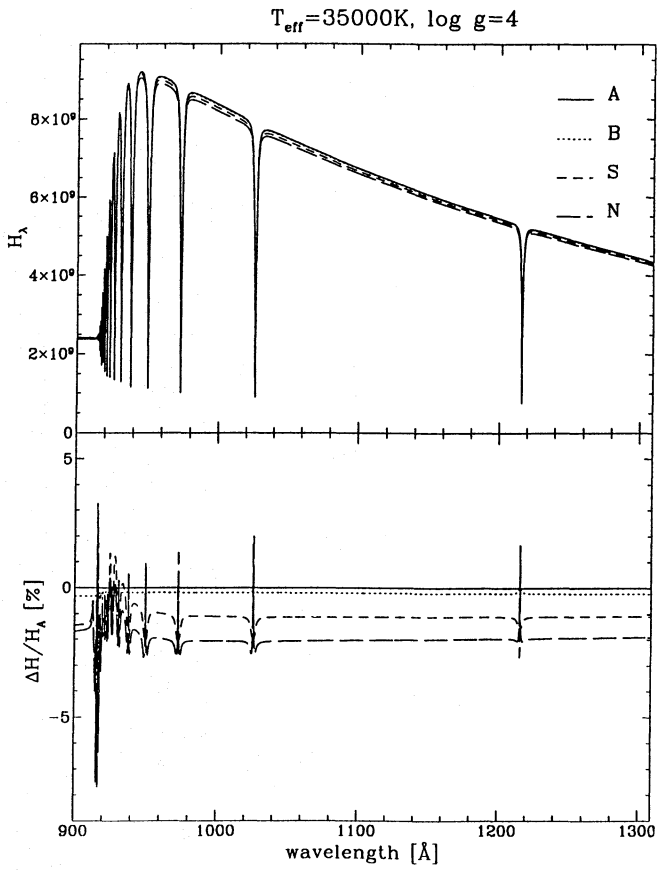

Fig. 11. An analogous plot as in Fig. 7, but for $T_{\rm eff}$= 35000 K, log g = 4

stellar atmospheres taking into account level dissolution and line-merging.

6. Conclusions

The basic goal of this paper was to show the extent to which the regions of line merging near the series limits influence the computed model stellar atmosphere structure and the predicted spectrum. To make our results as useful as possible, we have carefully examined the errors in spectral indicators resulting from neglecting the line merging altogether, and from using different treatments of these phenomenon. Based on our results, the user of a stellar atmosphere modeling code (such as TLUSTY) may choose a different level of sophistication (and therefore different demands on computer resources) according to the required accuracy of modeling, which in turn reflects the spectrophotometric accuracy of observations at hand.

Specifically, we ask the following question: what has to be included into the modeling procedure to achieve accuracy of all predicted spectral features to within 1 per cent, for a plane-parallel, pure-hydrogen model atmosphere in hydrostatic and radiative equilibrium? Although this question might seem trivial, our results demonstrate that this is far from true. We have deliberately limited ourselves to the simplest atmospheres, because without a proper understanding of this archetypical prob-

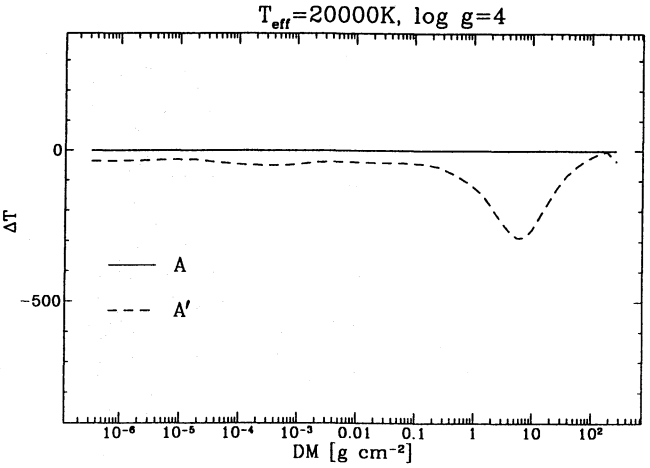

Fig. 12. Temperature difference between model A′ (analogous to model A, but Lyman lines have full profiles and frequency-dependent background opacity) and model A (cf. Fig. 4 - Lyman lines have half profiles and frequency-independent background opacity)

© European Southern Observatory • Provided by the NASA Astrophysics Data System

1994A&A...282..151H

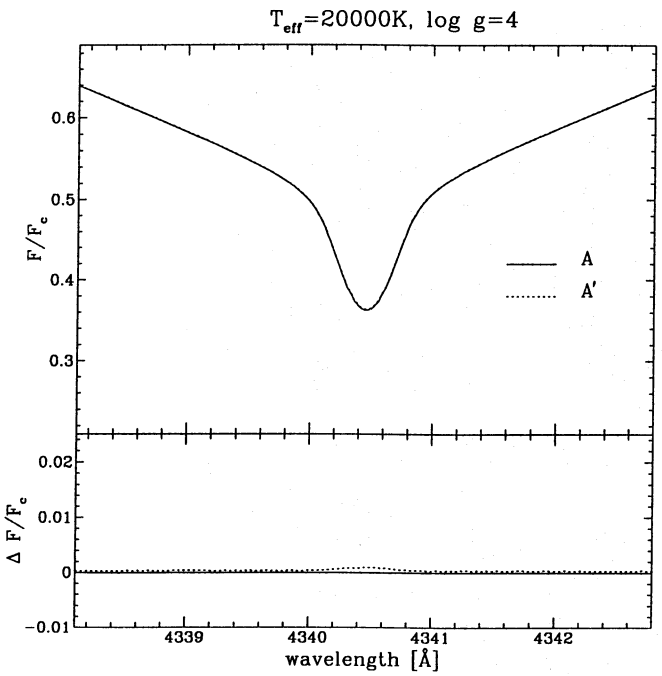

Fig. 13. The Hγ profiles (upper panel) and their difference (lower panel) for the models displayed in Fig. 12. Differences are hardly visible on the plot

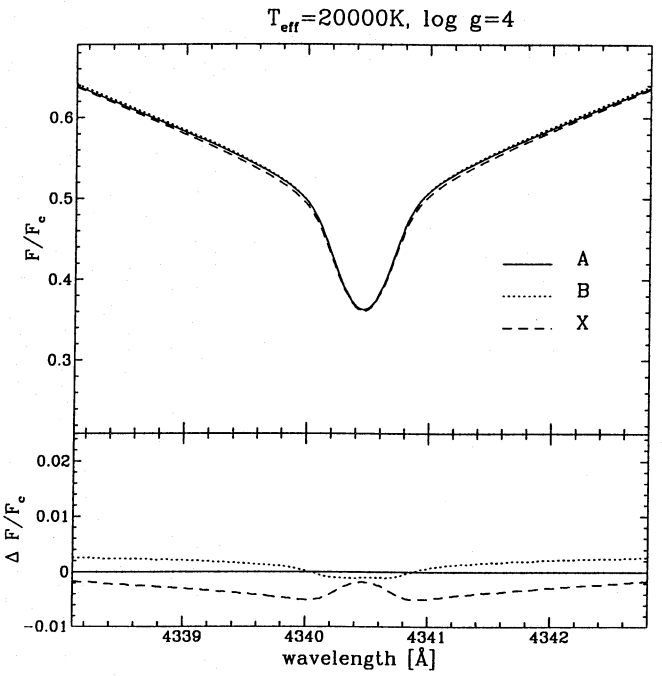

Fig. 15. The Hγ profiles (upper panel) and their differences (lower panel) for the models displayed in Fig. 14

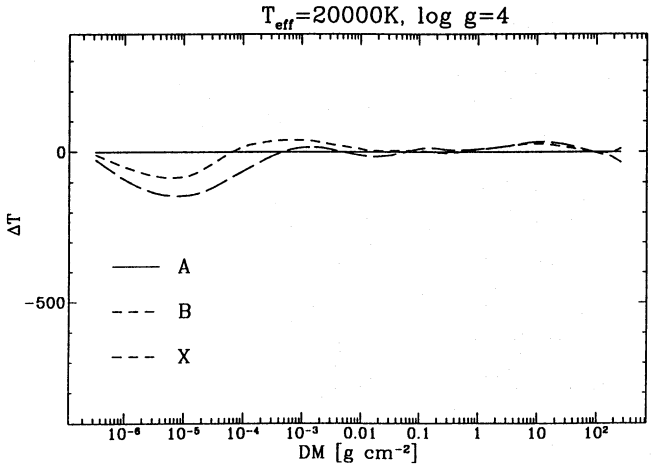

Fig. 14. Temperature differences between models A, B (cf Fig. 4), and X (analogous to A, but with 12 instead of 8 lowest levels treated explicitly)

lem one cannot hope to achieve significant progress in modeling more realistic stellar atmospheres.

An appropriate description of line merging involves two separate problems. First, the detailed physics of level dissolution has to be considered. Since this phenomenon is usually thought of in the context of high-density plasmas, all previous formalisms were limited to LTE situations. However, for NLTE stellar atmosphere models we must allow for the dissolution of Rydberg states without the LTE assumption. This development eliminates the necessity of adopting an arbitrary cutoff of the number of higher LTE levels, traditionally taken to be 16 (after Auer & Mihalas 1969). In fact, the number of levels taken into account is no longer a mark of quality of a particular model, because in our framework the number of effective levels varies throughout the atmosphere.

Second, the complicated shape of the opacity in the line merging regions causes significant numerical problems. To cope with this difficulty, we have generalized the concept of the opacity distribution function beyond its usual LTE context. We have implement this idea in two different ways by introducing the "line ODF" and the "continuum ODF". This also enables us to asses the internal accuracy of our statistical approach.

As an illustration of these techniques, we have calculated several pure hydrogen models atmospheres for two effective temperatures, $T_{\rm eff}$ = 20000 and 35000 K, and discussed the differences between models calculated with different treatments of the line merging opacity. In particular, we have shown that the errors in the predicted profiles of Balmer lines resulting from neglecting line merging are typically of the order of 3 - 4 %, while the errors in the far-UV portion of the Balmer continuum reach 15 - 35 %. The errors generally decrease with increasing effective temperature. At the same time, the internal accuracy of the models is shown to be about or below 0.5 % for all predicted spectral features.

The answer to the question posed above is that to obtain the 1 % accuracy level required for interpreting current spectrophotometric observations, models must include line merging. Fortunately, the formalism developed in this paper provides such an accurate and robust modeling technique.

© European Southern Observatory • Provided by the NASA Astrophysics Data System

1994A&A...282..151H

Acknowledgements. We are indebted to Dr. Keith Butler for the Balmer line broadening profiles. This work was supported in part by NASA grant No. 65 under program NRA 91–OSSA–12.

Appendix A: occupation probabilities

The occupation probability of level j is expressed in terms of the microfield distribution function $W(\beta; a, Z_r)$ by

$$w_j = Q(\beta_c(j)) \equiv \int_0^{\beta_c} W(\beta; a, Z_r)\, d\beta, \qquad \text{(A.1)}$$

where the quantity β_c is the critical field strength, and is given by (HM, Eq. 4.35)

$$\beta_c = 8.3 \times 10^{14}\, n_e^{-2/3}\, Z^3\, k\, j^{-4}, \qquad \text{(A.2)}$$

with

$$k = \begin{cases} 1, & \text{for } j \le 3; \\ (16/3)\, j/(1+j)^2, & \text{for } j > 3; \end{cases}, \qquad \text{(A.3)}$$

Here Z_r is the radiator charge (=0 for hydrogen), Z is the ionic charge and a is the correlation parameter, given by

$$a = 0.09\, n_e^{1/6}\, T^{-1/2}. \qquad \text{(A.4)}$$

For $a = Z_r = 0$ the microfield distribution function is given by the well-known Holtsmark distribution and the function $Q(\beta)$ can be accurately generated from a rational expression (Hummer 1986).

When plasma correlation effects are important, ie. when $a > 0$, the microfield distribution functions are those given, for example, by Hooper (1966). Using a substantially modified version of Hooper's code, T. Schöning and Hummer (unpublished) computed a two-dimensional fit to $W(\beta; a, Z_r)$ for $a \le 0.8$ and $Z_r = 0, 1, \ldots, 5$. From these fits the integral in (A.1) is easily evaluated. Typical results are shown in Fig. 16. The numerical results can be approximated by

$$w_j = f/(1+f), \qquad \text{(A.5)}$$

where

$$f = \frac{0.1402\,(x + 4\, Z_r\, a^3)\, \beta_c^3}{1 + 0.1285\, x\, \beta_c^{3/2}}, \qquad \text{(A.6)}$$

and

$$x = (1+a)^{3.15}, \qquad \text{(A.7)}$$

For $a = Z_r = 0$, the fit is particularly simple and is accurate to 2 %. The maximum error in general is of the order of 20 % except for very small β, where w_i is essentially zero.

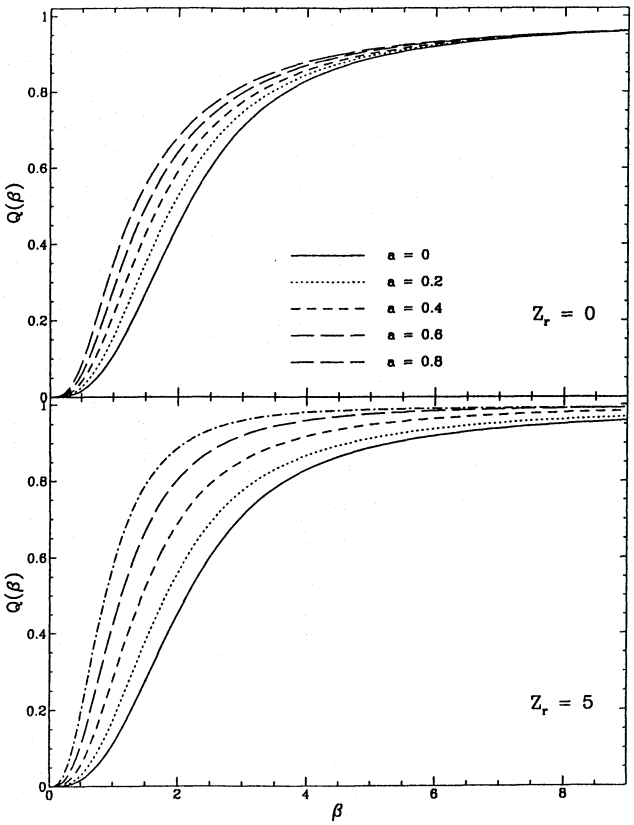

Fig. 16. The occupation probability function $Q(\beta; a, Z_r)$ for radiator charge $Z_r = 0$ and $Z_r = 5$, with indicated values of the plasma parameter a

Appendix B: details of line broadening

The opacity in a line $i \to j$ is

$$\chi_{ij}(\nu) = \left[w_j n_i - w_i n_j (g_i/g_j)\right] \sigma_{ij}(\nu), \qquad \text{(B.1)}$$

where the cross-section σ_{ij} is expressed through the normalized profile coefficients ϕ_{ij} by

$$\sigma_{ij}(\nu) = \frac{\pi e^2}{mc}\left[f_{ij}^S \phi_{ij}^S(\nu) + (f_{ij} - f_{ij}^S)\, \phi_{ij}^D(\nu)\right]. \qquad \text{(B.2)}$$

Here f_{ij} is the (total) oscillator strength, and f_{ij}^S the Stark oscillator strength, which is the part of the line f-value contributed by components displaced by an electric field (Underhill & Wadell 1959). These two f–values are equal when $(i+j)$ is even. The second term in Eq. (B.2) is the standard Doppler profile (we neglect resonance and natural broadening for simplicity, but these may be easily included if needed).

In the following, we will be concerned only with the Stark part of the profile. We found that the following approximation gives a simple and surprisingly accurate representation of the profile. This approach is implemented in the program TLUSTY. First, we express the distance form the line center through a convenient parameter β (after Griem 1960),

$$\beta = \frac{\Delta\lambda}{F_0 K_{ij}}, \qquad \text{(B.3)}$$

© European Southern Observatory • Provided by the NASA Astrophysics Data System

1994A&A...282..151H

where F_0 is the normal field strength, $F_0 = 1.25\times10^{-9}n_e^{2/3}$, and K_{ij} is the coefficient of the asymptotic Hotsmark profile, tabulated by Griem. Beyond the tabular values, we use the asymptotic formula

$$K_{ij} = 5.5\times10^{-4}\frac{i^4j^4}{j^2-i^2}, \qquad \text{(B.4)}$$

Next, we express the Doppler width in terms of β units, viz

$$\beta_D = \frac{c}{\nu_0^2F_0K_{ij}}\Delta\nu_D = \frac{1}{\nu_0F_0K_{ij}}\sqrt{\frac{2kT}{m_H}+v_{tb}^2}, \qquad \text{(B.5)}$$

where m_H is the atomic mass, and v_{tb} the microturbulent velocity. The quantity β_D expresses the relative importance of the Doppler and Stark broadening: the larger the β_D, the more dominant the Doppler broadening. Next, we introduce the Doppler and the asymptotic Holtsmark broadening functions,

$$\phi_D = \frac{1}{\sqrt{\pi}\beta_D}\exp[-(\beta/\beta_D)^2], \qquad \text{(B.6)}$$

and

$$\phi_H = 3\,\beta^{-5/2}. \qquad \text{(B.7)}$$

Equation (B.7) applies only for hydrogen lines where both electrons and protons contribute in the equal manner. For He II (and other hydrogenic) lines, where only electrons contribute, $\phi_H = (3/2)\beta^{-5/2}$. Here we are concerned only with hydrogen.

The next step is to find the value of β where both profiles have the same value, i.e to solve a transcendental equation

$$x^2 - (5/2)\ln x - C = 0, \qquad \text{(B.8)}$$

where $C = (3/2)\ln\beta_D - \ln(3\sqrt{\pi})$; and x is the usual dimensionless distance from the line center, $x = \beta/\beta_D = \Delta\nu/\Delta\nu_D$. Equation (B.8) follows on taking the logarithm of Eqs. (B.6) and (B.7) and equating their right hand sides.

As Eq. (B.8) has a solution only if $C \geq (5/4 - 5/2\ln 5/2)$, i.e. for $C \geq 0.97$, or $\beta_D \geq \beta_D^{\rm crit} = 5.82$, we consider two different regimes, $\beta_D \geq \beta_D^{\rm crit}$, and $\beta_D < \beta_D^{\rm crit}$ separately.

i) If $\beta_D \geq \beta_D^{\rm crit}$, Doppler broadening is dominant in the line core, and we may simply join the Doppler profile in the core and the asymptotic Holtsmark profile in the wing. Equation (B.8) for the division point has two real solutions. We take the larger one, denoted as β^*, because the smaller always lies in the Doppler core, and set the line profile coefficient to

$$\phi^S(\beta) = \begin{cases}\phi_D(\beta), & \text{if } \beta \leq \beta^*;\\ \phi_H(\beta), & \text{if } \beta > \beta^*.\end{cases}, \qquad \text{(B.9)}$$

The solution of Eq. (B.8) is very easily found by Newton's method, with the initial estimate $x_0 = \sqrt{C}[1+(5/4)\ln C/(4C-5)]$ for $C > 1.26$, and $x_0 = \sqrt{C+0.28}$ elsewhere. The iterations cycle is $x_{n+1} = x_n - P(x_n)/P'(x_n)$, where P is the l.h.s. of Eq. (B.8), and $P' = 2x - 5/2$ is its derivative. The procedure converges very rapidly, yielding a converged solution typically in two or three iterations. β^* is then given by $\beta^* = x_{\rm conv}\beta_D$.

ii) If $\beta_D < \beta_D^{\rm crit}$, Stark broadening is dominant everywhere, and in the first approximation the Doppler broadening may be neglected. Stark broadening may be approximated by an empirical formula which gives a reasonably accurate fit to the calculations of Edmonds et al. (1967), namely

$$\phi^S(\beta) = \begin{cases}0.08, & \text{if } \beta < 1.14;\\ a_0\exp[a_1\ln\beta + a_2(\ln\beta)^2], & \text{if } 1.14 \leq \beta < 11.4;\\ \phi_H(\beta), & \text{if } \beta \geq 11.4.\end{cases}, \qquad \text{(B.10)}$$

with $a_0 = 0.07209481$, $a_1 = 0.4796232$, $a_2 = 0.5758228$.

Finally, the usual profile coefficient in frequency units is given by

$$\phi(\Delta\nu) = \frac{c}{\nu_0^2F_0K_{ij}}\phi(\beta) \qquad \text{(B.11)}$$

References

Anderson L.S., 1989, ApJ 339, 558.
Auer L.H., Mihalas D., 1969, ApJ 158, 641.
Bergeron P., Wesemael F., Fontaine G., 1991, ApJ, 367, 253.
Carbon D. F., 1984, In: Methods in Radiative Transfer, Ed. Kalkofen W., Cambridge University Press, Cambridge, p. 395.
Däppen W., Anderson L.S., Mihalas D., 1987, ApJ 319, 195.
Dreizler S., Werner K., 1992, in The Atmospheres of Early Type Stars, Lecture Notes in Phys., Vol. 401, Eds. Heber U. & Jeffery S., Springer, Berlin, p. 270.
Edmonds F.N., Schlüter H., Wells D.C., 1967, Mem. R. Astr. Soc. 71, 271.
Fano U., Cooper J.W., 1968, Rev. Mod. Phys. 40, 441.
Griem H., 1960, ApJ 132, 883.
Hooper C.F., 1966, Phys. Rev. 149, 77.
Hubeny I., 1988, Comput. Phys. Commun. 52, 103.
Hubeny I., Lanz T., 1992a, A&A 262, 501.
Hubeny I., Lanz T., 1992b, BAAS 24, 1152.
Hummer D.G., 1986, JQSRT 36, 1.
Hummer D.G., Mihalas D., 1988, ApJ 331, 794.
Kudritzki R.P., Hummer D.G., 1990, ARA&A 28, 303.
Mihalas D., 1978, Stellar Atmospheres, Freeman, San Francisco.
Rauch T., Werner K., 1988, A&A, 202, 159.
Seaton M.J., 1990, J. Phys. B 23, 3255.
Underhill A.B., Wadell J.H., 1959, NBS Circular 603 (Washington: Government Printing Office).
Vidal C.R., Cooper J., Smith E.W., 1973, ApJS 25, 37.

This article was processed by the author using Springer-Verlag LaTeX A&A style file version 3.

© European Southern Observatory • Provided by the NASA Astrophysics Data System